

УДК 539.144.4

## MEMORY EFFECTS IN DISSIPATIVE NUCLEUS–NUCLEUS COLLISION

*H. L. Yadav, K. C. Agarwal*

Rajasthan University, Jaipur, India

A macroscopic dynamical model within the framework of a multidimensional Fokker–Planck equation is employed for a theoretical description of low-energy dissipative collisions between two heavy nuclei. The effect of two-body collisions leading to intrinsic equilibration has been treated phenomenologically using the basic concepts of dissipative diabatic dynamics. The heavy-ion reaction  $^{86}\text{Kr}$  (8.18 MeV/u) +  $^{166}\text{Er}$  has been used as a prototype to study and demonstrate the memory effects for dissipation and diffusion processes. Our calculated results for the deflection angle, angular distributions  $d\sigma/d\theta_{\text{cm}}$ , energy distributions  $d\sigma/d\Delta E$ , and element distributions  $d\sigma/dZ$  illustrate a remarkable dependence on the memory effects and are consistent with the experimental data.

Макроскопическая динамическая модель в рамках многомерного уравнения Фоккера–Планка применена для теоретического описания низкоэнергетического взаимодействия между ядрами. Эффект двухчастичных столкновений, приводящий к равновесию, был учтен феноменологически на основе диссипативной диабатической динамики. Реакция тяжелых ионов  $^{86}\text{Kr}$  (8,18 МэВ/а.е.м.) +  $^{166}\text{Er}$  использована как прототип для изучения эффектов памяти для диссипации и диффузии. Наши результаты для угла отклонения, углового распределения  $d\sigma/d\theta_{\text{cm}}$ , распределения энергии  $d\sigma/d\Delta E$  и распределения по элементам  $d\sigma/dZ$  дают заметную зависимость эффектов памяти и согласованы с экспериментальными данными.

### INTRODUCTION

Dissipative processes in heavy-ion reactions [1,2] with energies of a few MeV per nucleon above the Coulomb barrier are characterized by the dissipation of a large amount of kinetic energy and angular momentum of the relative motion into intrinsic excitations, as well as by the diffusion of nucleons between the two colliding nuclei [3,4].

The assumption of intrinsic equilibrium as produced by the residual two-body interactions, provides the common starting point of Markovian transport theories which have been used for the description of heavy-ion dissipative collisions [2, 3]. Obviously, such an assumption implies a small mean free path for the nucleons during the collision process. This, however, is not satisfied [5] in the initial stage (approach phase) of the reaction which is characterized by a long mean free path (a few times the nuclear diameter). Therefore, the applicability of Markovian-type transport theories is restricted to the damped stage of dissipative collisions [6, 7].

It has been suggested earlier to include within a transport theoretical approach [5,6] the main memory effects (non-Markovian effects) which are due to long mean free path of the nucleons. The underlying theory is referred to as dissipative diabatic dynamics (DDD) and provides a natural extension of the current Markovian transport theories. It ascribes [6, 8] elastoplastic properties to nuclear matter and supplies a link between the description of giant

vibrations (initial stage) and the overdamped motion (final stage of the reaction). Apart from the present approach, memory effects have been considered by several authors within the framework of linear response theory [9, 10], and the results obtained for the friction coefficients do indicate that the memory effects may not be negligible.

With the above in view, a detailed investigation of the reaction  $^{86}\text{Kr}$  (8.18 MeV/u) +  $^{166}\text{Er}$  has been carried out within a phenomenological approach to the basic elements of DDD [8, 11]. Our model uses a multidimensional Fokker–Planck equation which is modified as compared to the standard treatment to include the memory effects due to intrinsic equilibration process. A comparison of our calculated results for the observables such as angular distribution, energy distribution and mass distribution, etc. with the experimental data, indeed, shows a remarkable dependence of memory effects on these observables as described briefly in this communication.

## 1. PHENOMENOLOGICAL APPROACH OF DDD TO NUCLEUS–NUCLEUS COLLISION

The interplay between the collective degree of freedom and the single particle motion forms the main theme of DDD [5]. For an intermediate range of collective velocities, the dynamical coupling between collective and intrinsic motion is approximately described by scaling the single particle wave functions according to collective deformation [12]. Within the picture of adiabatic levels, this behaviour is essentially accounted for by the jumping approximation at all Landau–Zener crossings [13], i. e., by the diabatic approximation. This diabatic single particle motion leads to collective particle–hole excitations, which store the collective kinetic energy in a time reversible manner as a conservative diabatic potential. This energy is subsequently dissipated by two-body collisions leading to an equilibrium within the «intrinsic» single particle degrees of freedom. Due to this mechanism, the friction force in the collective equation of motion becomes retarded in time. The nonlocality in time of the friction kernel is determined by the intrinsic equilibration time  $\tau_{\text{intr}}$ . This elastoplastic behaviour of finite Fermi systems has been analytically derived by Nörenberg [6] in a model of interacting Fermi gas within moving walls. The main results of our concern are that for the quadrupole deformation of the collective variable  $q(t)$ , (i) the energy of the particle–hole excitations (elastic limit) is given by

$$\hbar\omega_0 = 66 A^{-1/3} \text{ MeV}, \quad (1)$$

which is identified with the isoscalar giant vibration, and (ii) the friction coefficient in the dissipative limit is given by

$$\xi = B_0\omega_0^2\tau_{\text{intr}}, \quad (2)$$

where  $B_0$  is the irrotational mass parameter for zero deformation. We use this result in conjunction with the numerical estimate of  $\tau_{\text{intr}}$  given by Bertsch [12] to obtain the friction coefficient for the deformation degree of freedom, later to be used in our trajectory calculations.

Microscopic calculations of the diabatic single particle states within a two-centre shell model have been carried out by Lukasiak et al. [14]. The general result of these calculations

is that the diabatic potential  $\Delta U_{\text{diab}}$  in the region of overlap depends essentially on the distance between the mass centres of the colliding nuclei, and only weakly on the deformation. More recently, similar diabatic two-centre shell model calculations have been carried out by Diaz-Torres et al. [15] for the study of dinuclear system in the context of fusion process in heavy-ion collisions at low energies. These microscopic calculations are quite involved. For extensive application to nucleus–nucleus collisions we, therefore, prefer here to use a phenomenological approach [8, 11] as prescribed earlier. According to Ref. [8, 11], the effect of intrinsic equilibration is treated through a time-dependent dynamical potential

$$U_{\text{dyn}}(\mathbf{q}) = U_{\text{ad}}(\mathbf{q})[1 - \chi(t)] + U_{\text{diab}}(\mathbf{q})\chi(t) = U_{\text{ad}}(\mathbf{q}) + (\Delta U)_{\text{diab}}(\mathbf{q})\chi(t). \quad (3)$$

The decay factor  $\chi(t)$  describes a smooth transition from the diabatic potential  $U_{\text{diab}}$  to the adiabatic potential  $U_{\text{ad}}$ . It is given by

$$\chi(t) = \exp\left(-\int_{t_0}^t dt' \tau_{\text{intr}}^{-1}(t')\right), \quad (4)$$

where  $t_0$  denotes a time well before the collision.

For the intrinsic equilibration time  $\tau_{\text{intr}}$ , we use the results of a calculation due to Bertsch [12]. Using  $\sigma = 40$  mb for the average nucleon–nucleon cross-section, and identifying the total excitation energy per particle  $\varepsilon^*$  of Ref. [12] with the sum of the dissipated energy (thermal energy)  $E_{\text{th}}^*$  and the energy stored in the diabatic potential  $(\Delta U(t))_{\text{diab}}$ , we obtain for the intrinsic equilibration time [12]

$$\tau_{\text{intr}} = (2.1 \cdot 10^{-22} \text{ s})A/[(\Delta U(t))_{\text{diab}} + E_{\text{th}}^*(t)]. \quad (5)$$

For typical heavy-ion reactions with total excitation energy  $\varepsilon^* \leq 0.5$  MeV, the intrinsic equilibration time is larger than  $4 \cdot 10^{-22}$  s. Thus, the intrinsic equilibration time  $\tau_{\text{intr}}$  is larger than the approach time  $\tau_{\text{appr}} \approx 2 \cdot 10^{-22}$  s from contact to turning point for a central collision. This estimate shows again that the assumption of intrinsic equilibrium is not correct during the approach phase of a nucleus–nucleus collision.

It is emphasized that our decay factor  $\chi(t)$  describes the transition from an ordered single particle motion, the initial diabatic motion, to a motion characterized by intrinsic equilibrium. Due to this fact, the  $\chi(t)$  not only enters the potential but also the transport coefficients. Furthermore, it should be noted that we treat the deformation (mean values and fluctuations) explicitly, and, therefore, our present study goes beyond the treatment of Refs. [8, 11].

The diabatic potential in Eq. (3) due to the diabatic single particle motion is parameterized as

$$(\Delta U)_{\text{diab}} = (\Delta U)_{\text{diab}}^0 F_{\text{diab}}(r) + (\Delta U(r, \varepsilon))_{\text{diab}}^{\text{def}}, \quad (6)$$

where the first term corresponds to the diabatic energy for the overlapping nuclei. The second term represents the potential energy of the giant quadrupole vibration for the individual nuclei. This potential is assumed to vanish for the compound nucleus shape and takes the appropriate values for the separated nuclei. The radial dependence  $F_{\text{diab}}(r)$  of the first term is derived from the square root of density overlap of the two nuclei [8, 16]. For convenience in numerical application the form factor is fitted to a Fermi distribution and is normalized to

unity at the centre ( $r = 0$ ) and falls off to zero for distances beyond the interaction radius. The strength of the diabatic potential has been obtained earlier in Ref. [11] at the compound nucleus shape from the schematic consideration of the two-centre shell model calculations and has been successfully applied for the description of heavy-ion collisions including fusion and fast fission [11]. It was used subsequently in Ref. [8] for a preliminary study of heavy-ion reactions within the framework of a multidimensional Fokker–Planck equation and is given by

$$(\Delta U)_{\text{diab}}^0 = 60A_1^{1/3}A_2^{1/3}/(A_1^{1/3} + A_2^{1/3}) \text{ MeV}, \quad (7)$$

where the proximity form for the mass asymmetry dependence has been used. For the  $^{86}\text{Kr} + ^{166}\text{Er}$  system this gives  $(\Delta U)_{\text{diab}}^0 = 147 \text{ MeV}$ . The second term of Eq. (6) is parameterized as

$$(\Delta U(r, \varepsilon))_{\text{diab}}^{\text{def}} = \frac{1}{2}(C_1 + C_2)\varepsilon^2(1 - G_{\text{diab}}(r)), \quad (8)$$

wherein the deformation parameter  $\varepsilon$  describes axially symmetric quadrupole deformation. The stiffness coefficients  $C_1$  and  $C_2$  are obtained from the experimental value  $E_i = 63A_i^{1/3}$  for the quadrupole giant vibration using the relation  $E_i = \hbar(C_i/B_i)^{1/2}$  with the irrotational mass parameter  $B_i$  for the individual nuclei  $i = 1, 2$ . For compact shapes, the distance  $r$ , and the deformation  $\varepsilon$  defined through the ratio of the major to minor axes are no more independent variables. And thus, in order to avoid double counting, we keep only the first term in Eq. (6) to define the diabatic potential for compact shapes. This is achieved through an appropriate form factor  $G_{\text{diab}}(r)$ . Altogether the parameters of the diabatic part of the potential, Eq. (6), are chosen such that we get a realistic description from well separated nuclei down to compact shapes of the collision complex.

In Fig. 1 we have plotted our phenomenological diabatic potential for the  $^{86}\text{Kr} + ^{166}\text{Er}$  system as a function of distance  $r$  for zero deformation [ $(\Delta U(r, \varepsilon))_{\text{diab}}^{\text{def}} = 0$ ]. A corresponding potential obtained in a microscopic description using the diabatic two-centre shell model is also shown in Fig. 1 for the purpose of comparison. One observes that, except for small distances  $r < 8 \text{ fm}$ , the two potentials have similar features. We emphasize that such a phenomenological diabatic potential has been tested earlier to provide a reasonably good description [11] of heavy-ion collisions including the fusion and fast fission. Guided by its success, we have preferred to use this potential instead of other successfully employed

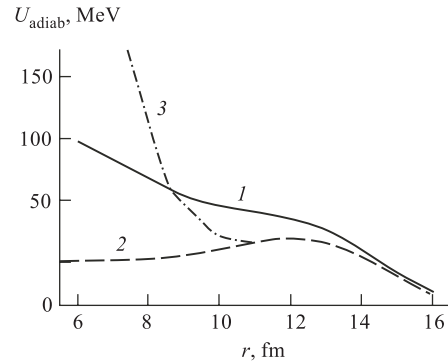


Fig. 1. The solid line (1) depicts the phenomenological diabatic potential  $U_{\text{diab}}^{\text{phen}}$  for zero deformation ( $\varepsilon = 0$ ), obtained by adding to the adiabatic potential  $U_{\text{adiaab}}$ , shown by the dashed line (2), the  $(\Delta U)_{\text{diab}}$  according to Eqs. (3) and (6). A corresponding potential  $U_{\text{diab}}^{\text{micr}}$  obtained in a microscopic calculation [14] using the diabatic two-centre shell model has been shown by the dash-dotted line (3) for the purpose of comparison

phenomenological potentials like, for example, the adiabatic folding potentials used for the dinuclear system model of fusion [15]. The difference between the microscopic and phenomenological potentials in Fig. 1 at smaller distances, indeed, for our practical calculations, does not matter. This is because the interior region is seen only by the central trajectories for small impact parameters, whose contribution to the total cross-section is insignificant. A small difference at the barrier between the phenomenological and the microscopic potentials is expected to influence slightly the trajectories which are able to probe the barrier region. However, from our earlier calculations [8], wherein effect of variation of intrinsic equilibration time  $\tau_{\text{intr}}$  on the angular and energy distributions has been studied in detail, we find that this does not make any significant change in our calculated results for the various cross-sections. Thus, for extensive applications of DDD, it is numerically much less involved to employ the phenomenological approach as described in this section and we have chosen it for our extensive studies reported here.

## 2. FORMULATION OF THE MODEL

As relevant collective variables describing the collision complex, we choose the relative distance  $r$  between the two nuclei, the angle of rotation  $\theta$ , the mass asymmetry  $\alpha$  and the deformation  $\varepsilon$ . The conjugate momenta corresponding to these variables are the relative radial momentum  $p$ , the angular momentum  $l$  for rotation and the momentum  $\pi$  for the deformation variable  $\varepsilon$ . In terms of the fragment mass numbers  $A_1$ ,  $A_2$  and the total mass of the system  $A = A_1 + A_2$ , the mass asymmetry is defined by  $\alpha = (A_2 - A_1)/A$ . In our parameterization of the shapes we allow only symmetric deformations. We define the deformation  $\varepsilon$  for such symmetric shapes in terms of the eccentricity  $\eta$  as  $\varepsilon = \eta^{2/3} - 1$ .

In the phenomenological approach to the memory effects implied by the intrinsic equilibration process as described in Sec. 1, we use the following form of the Fokker–Planck (FP) equation:

$$\begin{aligned} \partial f / \partial t + \sum_i [(p_i / m_i) \partial f / \partial q_i + (\partial U_{\text{dyn}} / \partial q_i) \partial f / \partial p_i] = \\ = - \sum_i \partial (v_i f) / \partial p_i + \sum_{i,j} \partial^2 (D_{ij} f) / \partial p_i \partial p_j \end{aligned} \quad (9)$$

for the multidimensional distribution function  $f(q_i, p_i, t)$ , where  $p_i$  are the conjugate momenta of the collective coordinates  $q_i$ . Here we exclude for the moment the mass asymmetry degree of freedom which is treated differently as explained below. The mass tensor is assumed to be diagonal in the chosen collective degrees of freedom. Instead of the adiabatic potential in the commonly used FP equation, the explicitly time-dependent dynamical potential (3), given below, with  $U_{\text{dyn}}^{\text{pot}}$  defined in Sec. 1 enters

$$U_{\text{dyn}} = T(p_i, q_i) + U_{\text{dyn}}^{\text{pot}}. \quad (10)$$

Here  $T(p_i, q_i) = p_i^2 / 2m_i$  denotes the kinetic energies for different degrees of freedom (translational, rotational, etc.). The transport coefficients, i. e., drift coefficients  $v_i$  and diffusion coefficients  $D_{ij}$  become also explicitly time-dependent due to finite equilibration within the intrinsic degrees of freedom.

The numerical solution of the FP equation (9) for the multidimensional probability distribution is not practicable. Alternatively, we have employed the moment expansion [1, 8] up to second order which yields a set of coupled differential equations describing the mean values and fluctuations. These equations of motion are eventually used for the trajectory calculations.

**2.1. Inclusion of Mass Diffusion, Overdamped Motion.** If we describe the transfer of nucleons between the colliding nuclei quantum mechanically and reduce this description by statistical considerations to an FP equation, we find [3, 17] that, in addition to the drift and diffusion terms on the r. h. s. of Eq. (9), there appear terms with  $D_{i\alpha}$ ,  $D_{\alpha,i}$  and  $v_{\alpha}$ , whereas the l. h. s. remains unchanged. Formally, we can use the general moment expansion discussed above by including the momentum degrees of freedom corresponding to  $\alpha$  and taking  $m_{\alpha} \rightarrow \infty$  and  $\partial U_{\text{dyn}}/\partial q_{\alpha} \rightarrow 0$ . This limit is known as overdamped motion and is generally assumed for dissipative collisions.

**2.2. Potential Energies and Transport Coefficients.** For the adiabatic potential energy  $U_{\text{ad}}(r, \alpha, \varepsilon)$  appearing in the dynamical potential  $U_{\text{dyn}}$ , Eq. (10), we follow Möller and Nix [18] to parameterize nuclear shapes in terms of collective coordinates  $r, \alpha$ , and  $\varepsilon$  of our model. In terms of these variables the macroscopic potential energy is given as a sum of a Coulomb energy  $E_{\text{Coul}}(r, \alpha, \varepsilon)$  and a nuclear potential energy  $E_{\text{nucl}}(r, \alpha, \varepsilon)$  calculated within the liquid drop model [18]. As typical examples of potential energy curves we have shown in Figs. 2 and 3 the results of  $U_{\text{ad}}$  as a function of  $(r/R_0)$ , where  $R_0$  is the equivalent radius

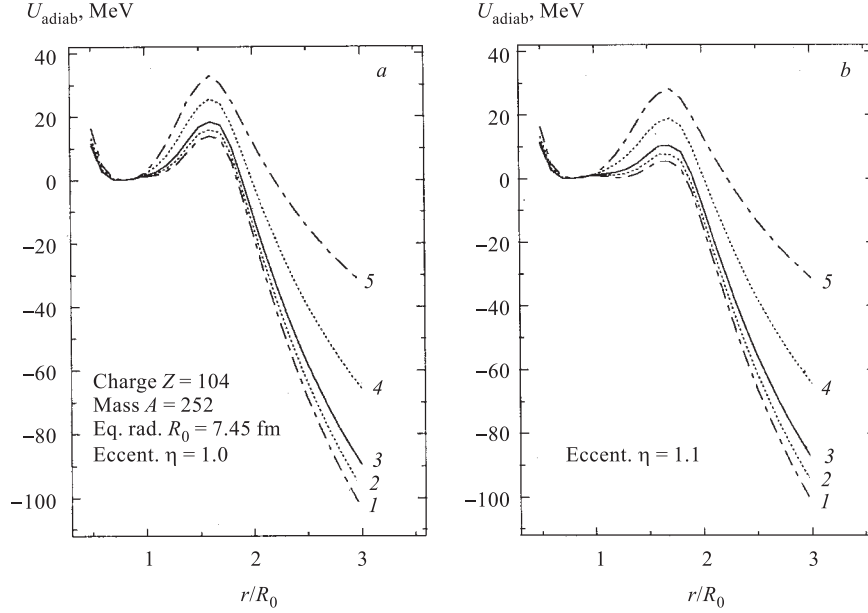


Fig. 2. Potential energy  $U_{\text{adiab}}$  as a function of  $r/R_0$ , where the equivalent compound nucleus radius  $R_0 = 7.45$  fm. The two plots show the variation of potential energy calculated for two fixed values of deformation  $\varepsilon = 0.0$  (a) and  $0.065$  (b), respectively, with five different mass asymmetry values  $\alpha = 0.0$  (1),  $0.2$  (2),  $0.3$  (3),  $0.5$  (4) and  $0.7$  (5) covering the entire range of  $\alpha$  values actually encountered in our trajectory calculations

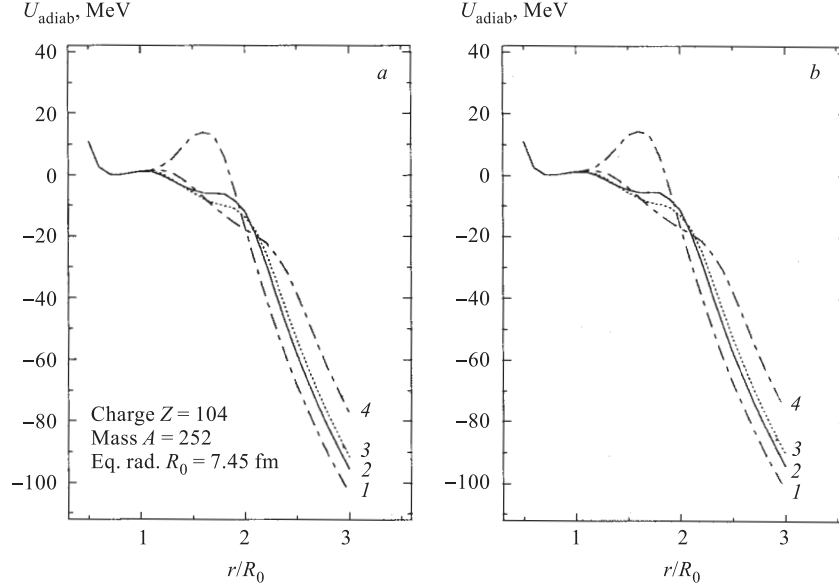


Fig. 3. The two plots, as in Fig. 2, show the variation of potential energy calculated for two fixed values of mass asymmetry  $\alpha = 0.0$  (a) and  $0.1$  (b), respectively. For each case, potential energy curves for four different values of deformation  $\varepsilon = 0.0$  (1),  $0.19$  (2),  $0.25$  (3) and  $0.37$  (4) covering typical range of values actually encountered in our trajectory calculations have been drawn

of the compound nucleus defined through the volume conservation. The two plots in Fig. 2 depict the results for different values of mass asymmetry ranging from  $\alpha = 0.0$  to  $0.70$  for the fixed value of deformation  $\varepsilon = 0.0$  ( $\eta = 1.0$ ) (Fig. 2, a) and  $\varepsilon = 0.065$  ( $\eta = 1.1$ ) (Fig. 2, b), respectively. Similarly the two plots in Fig. 3 show analogous results for different values of deformation  $\varepsilon = 0.0$  ( $\eta = 1.0$ ),  $\varepsilon = 0.19$  ( $\eta = 1.3$ ),  $\varepsilon = 0.25$  ( $\eta = 1.4$ ), and  $\varepsilon = 0.37$  ( $\eta = 1.6$ ) for fixed values of mass asymmetry  $\alpha = 0.0$  (Fig. 3, a) and  $\alpha = 0.10$  (Fig. 3, b), respectively.

The transport coefficients  $v_i$  and  $D_{ij}$  appearing in the equation of motion for the mean values and fluctuation depend on the collective variables  $\alpha$ ,  $r$  and  $\varepsilon$  as well as explicitly on the time. In parameterizing them, we write

$$v_i = v_i^0 f_i(r, \varepsilon) g_i(t), \quad (11)$$

$$D_{ij} = D_{ij}^0 F_{ij}(r, \varepsilon) G_{ij}(t), \quad (12)$$

where the time factors  $g_i(t)$  and  $G_{ij}(t)$  have to be chosen in accordance with the intrinsic equilibration process. As in the case of diabatic potential, the form factors  $f_i(r, \varepsilon)$  and  $F_{ij}(r, \varepsilon)$  are given by the square root of the density overlap normalized at the contact radius [16]. For convenience in numerical application the density overlap form factor thus obtained is fitted to a Fermi distribution. The transport coefficients  $v_i^0$ ,  $D_{ij}^0$  for  $i, j = \{\alpha, l, p\}$  at the contact radius  $r_{\text{cont}}$  are obtained from Ref. [3, 17]. The transport coefficients  $v_\pi$  and  $D_{\pi\pi}$  for the deformation degree of freedom are obtained from Eq. (2) for the friction coefficient  $\xi$  (in the

dissipative limit),

$$v_\pi = -\pi\xi/B_0, \quad (13)$$

$$D_{\pi\pi} = \xi T, \quad (14)$$

where  $T$  denotes the temperature, and we have used the Einstein relation connecting the drift and diffusion coefficients. For the evaluation of  $\xi$  in (2) we use the intrinsic equilibration time  $\tau_{\text{intr}}$  determined by Eq. (5), the mass parameter  $B_0$  of the composite system, and the energy  $\hbar\omega_0$  for the isoscalar giant resonance given in Eq. (1).

The intrinsic equilibrium process is characterized by the time constant  $\tau_{\text{intr}}(t)$ . Like in the time dependence of the diabatic part of the potential energy, the decay factor  $\chi(t)$  given by Eq. (4) is assumed to determine the time dependence of the transport coefficient. This implies that the factors  $g_i(t)$  and  $G_{ij}(t)$  in Eqs. (11), (12) take the form  $(1 - \chi(t))$  enabling a smooth transition to dissipative transport process after the intrinsic equilibrium has been fully reached. In this respect, the situation for the tangential and radial motion for the grazing collisions is slightly different. In fact, the diabatic motion of single particle states makes sense only for central collision. Thus, it may be justified to remove the diabatic potential for the grazing collision. But the value of the cut-off angular momentum, above which the diabatic potential should be switched off, cannot be precisely determined.

In view of the above discussion, we have carried out three different sets of calculations:

(i) The first set of calculations excludes the diabatic potential for the angular motion due to the reasons discussed above. Thus, all the form factors  $g_i(t)$  and  $G_{ij}(t)$  are multiplied by the factor  $(1 - \chi(t))$ , excepting those related to the angular motion like  $(G_{\ell\ell}, G_{\ell\alpha}, \text{etc.})$ , and the results describing such elastoplastic processes have been denoted by ELPL1.

(ii) In another set of calculations we include the diabatic potential also for the angular motion, and the corresponding results have been described by ELPL2. This set of calculations employs the  $(1 - \chi(t))$  factor for all  $g_i(t)$  and  $G_{ij}(t)$ .

(iii) A third set of calculations is carried out without any consideration to the diabatic potential and describes the dissipative limit of the collision process. The results thus obtained are designated by DISLIM.

### 3. CALCULATIONS AND RESULTS

The equations of motion have been solved numerically for various impact parameters in a bin of 0.1 fm starting from that for the grazing collisions up to impact parameter  $b = b_{\text{cap}}$  for the captured trajectory. The impact parameter for the grazing trajectory is defined through  $b_{\text{gr}} = R_{\text{int}}[1 - V(R_{\text{int}})/E_{\text{cm}}]^{1/2}$ , where the interaction radius is empirically [2] given by  $R_{\text{int}} = [1.36(A_1^{1/3} + A_2^{1/3}) + 0.5]$  fm. For the initial relative distance between ions, we take  $r \approx 20$  fm well out of the interaction region. The initial values of the momentum and deflection angle are those given by the Coulomb trajectory. All the second moments (variances)  $\sigma_{q_i, q_j}^2$ ,  $\sigma_{q_i, p_j}^2$ ,  $\sigma_{p_i, p_j}^2$  are assumed to be zero in the beginning of the reaction. Moreover, we consider only the spherical shapes to start with. Calculations in the exit channel are continued up to a distance  $r$  well outside the interaction region. Beyond the interaction zone the time evolution of the trajectory is affected by the Coulomb interaction only. For the calculation of the cross-sections, the asymptotic distribution  $f(r \rightarrow \infty, p^\infty)$ ,

$\theta^\infty, \dots$ ) is obtained by transforming the distribution  $f(r, p, \theta, \dots)$  calculated at the finite distance  $r > R_{\text{int}}$  (interaction radius) according to known Coulomb trajectories.

**3.1. Trajectories.** Amongst the three sets of calculations described earlier, the ELPL1 case provides the most realistic description of collision process as would be seen from a comparison of the experimental data on the angular distribution  $d\sigma/d\theta_{\text{cm}}$ , energy distribution  $d\sigma/d\Delta E$  for the kinetic energy loss, and element distributions  $d\sigma/dZ$  described below. Therefore, in order to save space, we present here only the results of the ELPL1 case for our trajectory calculations.

The time evolution of different collective coordinates ( $r, p, \ell, \varepsilon, \alpha$ ) has been displayed in Figs. 4, 5 and 6 for a few chosen impact parameters  $b = 1.3, 3.0, 5.0, 7.0$  and  $9.0$  fm describing the entire range of possible initial relative angular momentum of the colliding nuclei. Figure 5 also depicts the variation of kinetic energy loss as a function of time for the above-mentioned impact parameters. Our results for trajectory calculations show that for large impact parameters  $b \approx 9.9$  fm, corresponding to grazing collision, the interaction time is expectedly very small, of the order of  $10^{-22}$  s. With gradual decrease of impact parameter  $b$  the interaction time increases and becomes quite large, of the order of  $10^{-21}$  s for relatively small  $b$  ( $\approx 6$  fm) values. For still smaller  $b$  values, the interaction time grows rapidly. For example, trajectories corresponding to  $b \approx 1.3$  fm have rather long reaction times  $\approx 300 \cdot 10^{-22}$  s, and the system appears to approach fusion. Consequently, for such

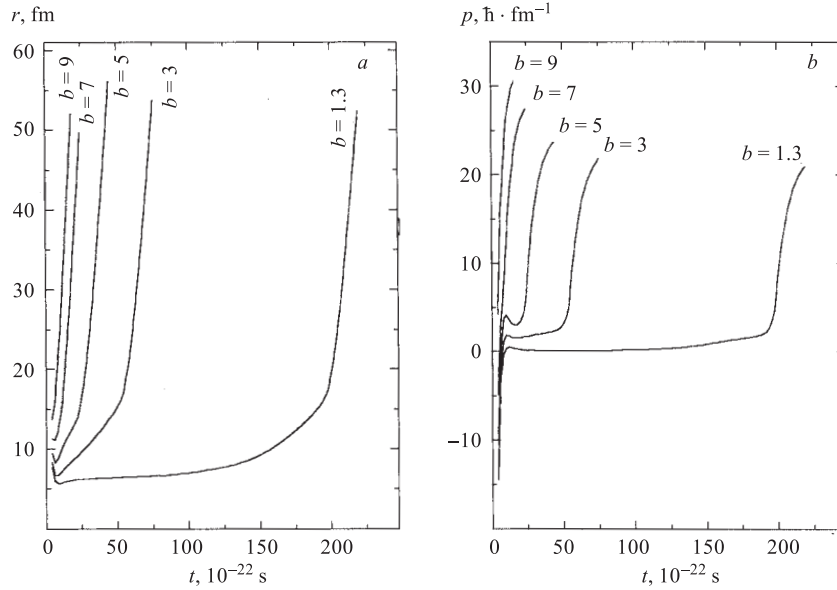


Fig. 4. The two plots show, respectively, the calculated trajectories with different impact parameter for the mean values of the radial coordinate  $r$  (a) and momentum  $p$  (b) as a function of time  $t(10^{-22}$  s). The trajectory corresponding to  $b = 1.3$  fm is a representative example of creeping motion during which the average value of momentum remains close to zero. These calculations along with those shown in Figs. 5 and 6 correspond to the elastoplastic case designated by ELPL1, as explained in the text

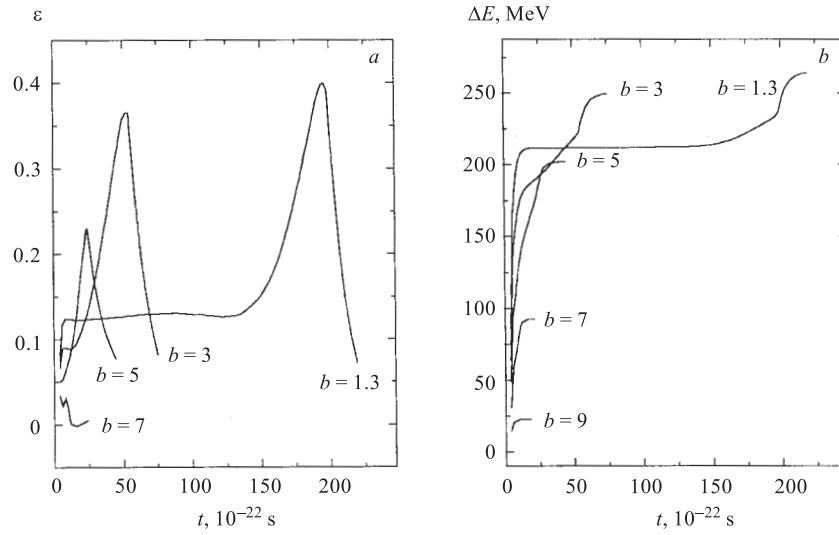


Fig. 5. As in Fig. 4, the plots show the trajectories for the time evolution of deformation  $\varepsilon$  (a) and the kinetic energy loss  $\Delta E$  (b) for a few selected impact parameters  $b$ . In the case of creeping trajectories the two nuclei remain within their interaction zone for a longer time and, therefore, develop rather large deformations. Already a large fraction of total kinetic energy loss occurs before the evolution of full deformation takes place

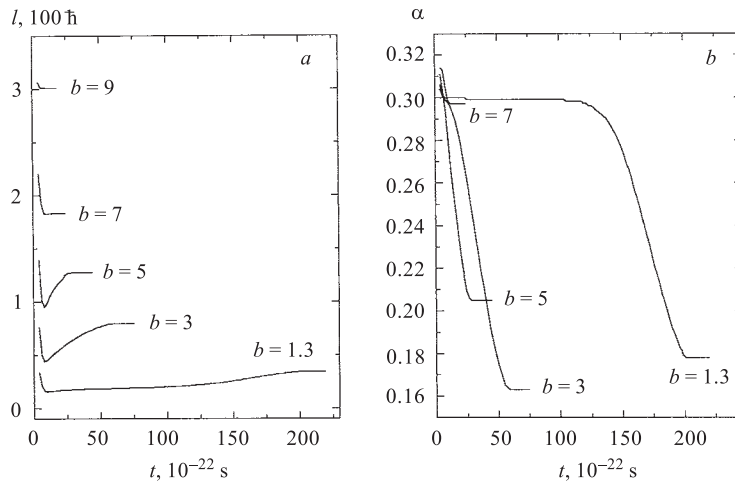


Fig. 6. As in Figs. 4 and 5, the plots depict the trajectories describing the time evolution of angular momentum  $\ell$  (a) and mass asymmetry  $\alpha$  (b) for a few selected impact parameters  $b$ . With increasing interaction time the system tends to move towards mass symmetry, as is evident from plot b

trajectories as seen in Fig. 4, *b* the radial momentum remains almost close to zero throughout until long time after which the nuclei separate away from each other. For such creeping trajectories during the long time of interaction the system develops large deformation of the order of  $\varepsilon \approx 0.4$ , as is seen in Fig. 5, *a*. The mass asymmetry for such creeping trajectories, as can be seen from Fig. 6, *b*, tends towards smaller values rather slowly as compared to those with intermediate values for the impact parameter around  $b = 3$  fm to  $b = 5$  fm.

The energy loss as a function of time displayed in Fig. 5, *b* shows that as the interaction time increases the kinetic energy loss grows and a substantial loss already takes place for the aforesaid intermediate values of impact parameter around  $b = 5$  fm for which the interaction time is only about  $10.0 \cdot 10^{-22}$  s. The change in relative angular momentum  $\ell$  with time for different impact parameters depicted in Fig. 6, *a* shows somewhat similar behaviour. However, trajectories corresponding to large initial  $\ell$  values exhibit relatively a larger amount of angular momentum loss in a short time as compared to the cases of very small impact parameters representing creeping motion.

It is found from our calculations that the method of moment expansion for the solution of FP equation breaks down for small impact parameters as reported in Ref. [8]. Such a difficulty in employing the moment expansion has also been encountered by Nix [19]. Since the inclusion of next higher-order terms in the moment expansion would not solve the difficulty, we have used an approximate method [8] in terms of reduced distribution function in calculating the second moments for the creeping trajectories, as described in detail in Ref. [8]. The values of the impact parameters below which the reduced distribution has been used can be easily seen from the point of discontinuity in Figs. 7, *b*, 9, *b* and 11, *b*, as described in the following.

**3.2. Mean Values, Variances and Differential Cross-Sections.** In Figs. 7–12 we have shown the mean values for the deflection angle defined through  $\theta_{\text{cm}} = \pi - \langle \theta \rangle$ , kinetic energy loss  $\Delta E$  and charge  $Z$ , as well as the associated variances  $\sigma_{\theta_{\text{cm}}\theta_{\text{cm}}}^2$ ,  $\sigma_{\Delta E\Delta E}^2$  and  $\sigma_{ZZ}^2$  along with the corresponding results for the differential cross-sections for the three different cases (i) ELPL1, (ii) ELPL2 and (iii) DISLIM distinguished by solid, dashed and dotted lines, respectively. In Figs. 8, 10 and 12 for the cross-sections we have also displayed the experimental differential cross-sections for the angular, energy and element distribution taken from Ref. [3]. As the present study pertains to a description of dissipative processes, we have excluded from our calculations of differential cross-sections the quasi-elastic region of energy loss, which corresponds to  $\Delta E = 15$  MeV for the reaction under consideration [3].

First, we consider the impact parameter dependence of the deflection angle. From Fig. 7, *a* one observes that in the case of ELPL1 and ELPL2, due to the extra repulsion from the diabatic potential, the range of impact parameters for which the deflection angle  $\theta_{\text{cm}}$  remains positive increases. In contrast, for the case of dissipative limit shown by dotted lines the angle  $\theta_{\text{cm}}$  decreases. On the other hand, during the time interval of intrinsic equilibration  $\tau_{\text{intr}}$ , the friction forces are not fully operative in the ELPL1 and ELPL2 cases due to the  $(1 - \chi(t))$  factor. Because of this with increasing  $\tau_{\text{intr}}$  the system loses its kinetic energy and angular momentum at a smaller rate as compared to that for the dissipative limit. Consequently, for the ELPL1 and ELPL2 cases the minimum distance of approach for the two nuclei decreases with increasing intrinsic equilibration time. For very small impact parameters and with no diabatic potential (DISLIM case), the interpenetration of two nuclei leads even to positive angle of deflection in contrast to the other two cases ELPL1 and ELPL2 wherein the diabatic potential is included for the description of the collision process. Further, in the ELPL1 case

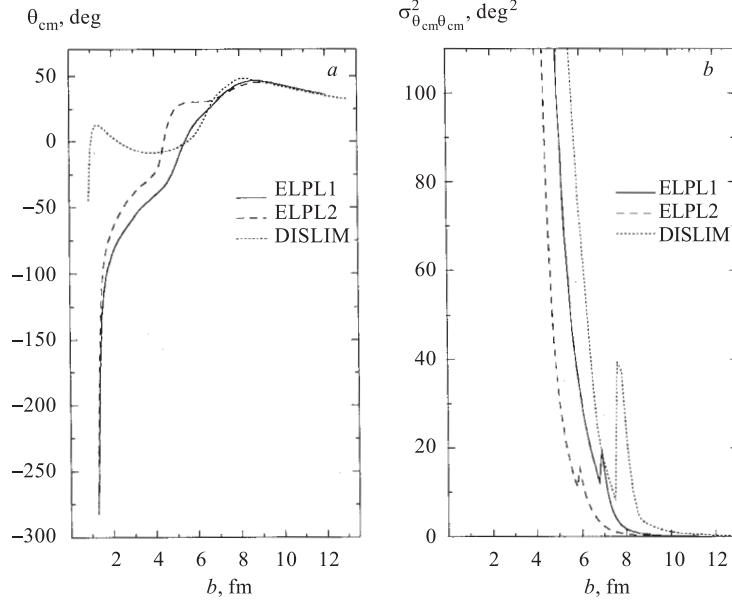


Fig. 7. The impact parameter  $b$  dependence of the mean deflection angle  $\theta_{cm}$  (a) and the associated variance  $\sigma_{\theta_{cm}\theta_{cm}}^2$  (b) for the three sets of calculations referred to as elastoplastic cases (1) ELPL1 and (2) ELPL2, and the case of dissipative limit (3) DISLIM, as described in the text. The minimum value of impact parameter for each set of calculation corresponds to the captured trajectory

the  $(1 - \chi(t))$  factor is not operative for the angular motion, and hence, the dissipation of angular momentum takes place at a faster rate as compared to that in the ELPL2 case. This in turn for the ELPL2 case increases the duration for which the deflection angle  $\theta_{cm}$  remains positive. In the case of smaller impact parameters  $b$  for which the interaction time is relatively large, the ELPL1 and ELPL2 results have similar features leading to large negative deflection angle.

Almost similar arguments hold good for the impact parameter dependence of the variance  $\sigma_{\theta_{cm}\theta_{cm}}^2$  displayed in Fig. 7, b. The discontinuity in the figure indicates the value of impact parameter below which the reduced distribution function is used for the calculations of variance as stated above. This discontinuity is seen to occur at around  $b = 6.8$  fm for ELPL1, at around  $b = 5.8$  fm for ELPL2 and at around  $b = 7.6$  fm for the DISLIM case. In the DISLIM case due to absence of the diabatic repulsive potential the proximity of the two nuclei increases, and one observes a much faster growth in the variance  $\sigma_{\theta_{cm}\theta_{cm}}^2$  with decreasing impact parameter as compared to that in the ELPL1 and ELPL2 cases.

Measurements [3, 20, 21] for the reaction  $^{86}\text{Kr}$  (8.18 MeV/u) +  $^{166}\text{Er}$  show that the deflection angle becomes negative for the completely damped components. From the plot  $a$  for mean values for deflection angle  $\theta_{cm}$  in Fig. 7, it is seen that this result corresponds to the elastoplastic case ELPL1 or ELPL2 and rules out the alternative possibility of the case for dissipative limit DISLIM. A comparison of our results with this feature of the experimental data clearly illustrates the memory effects. Consideration of the total area under

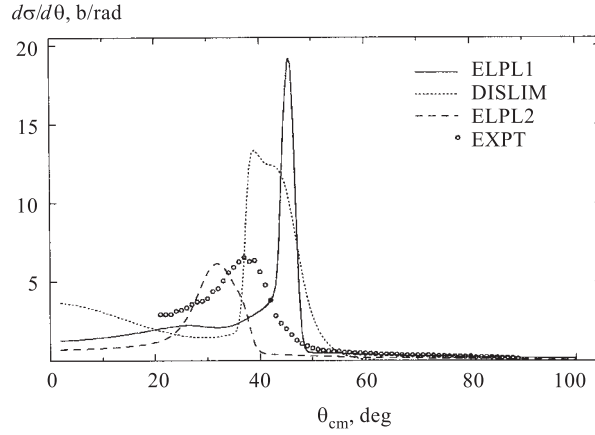


Fig. 8. Results for the angular distribution  $d\sigma/d\theta_{cm}$  for the three sets of calculations referred to as elastoplastic cases (1) ELPL1 and (2) ELPL2, and the case of dissipative limit (3) DISLIM, as in Fig. 7. These have been compared with the measured [3] angular distribution  $d\sigma/d\theta_{cm}$  wherein the quasi-elastic part of the reaction corresponding to energy loss  $\Delta E \leq 15.0$  MeV has been excluded, as explained in the text

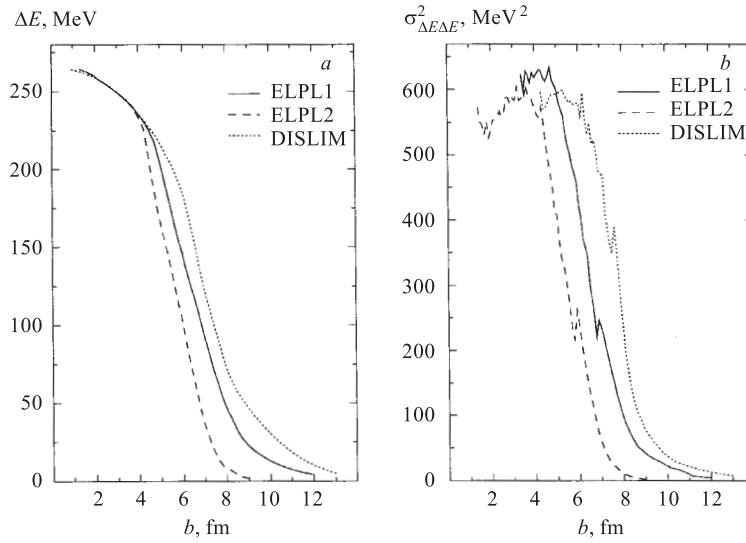


Fig. 9. The two plots, similar to Fig. 7, correspond to the mean energy loss  $\Delta E$  (a) and the associated variance  $\sigma_{\Delta E \Delta E}^2$  (b)

the experimental curve for the cross-section  $d\sigma/d\theta_{cm}$  shown in Fig. 8 also suggests that the ELPL1 and ELPL2 curves are closer to the measurements, though the peaks for corresponding angular distributions are slightly shifted as compared to the experimental peak.

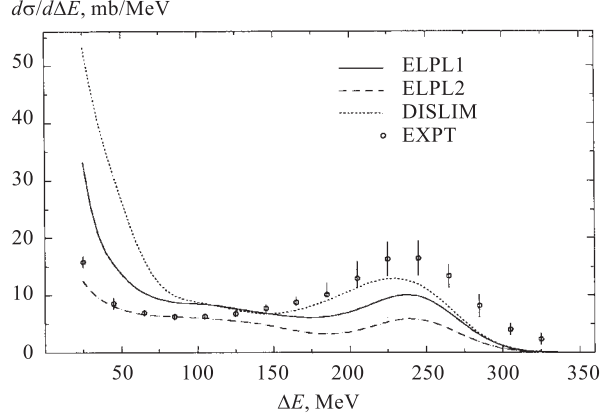


Fig. 10. Similar to Fig. 8, a comparison of the calculated energy distribution  $d\sigma/d\Delta E$  with the experimental data [3]

Our calculated results for the mean energy loss  $\Delta E$  and associated variances  $\sigma_{\Delta E \Delta E}^2$  are displayed in Fig. 9, whereas those for the energy distribution  $d\sigma/d\Delta E$  are shown in Fig. 10. In the DISLIM case, as explained above, due to the absence of repulsion from the diabatic potential, the two nuclei come into interaction zone of each other already for relatively larger impact parameters. This causes greater energy loss as compared to the ELPL1 and ELPL2 cases. Also in the case of ELPL1 the loss of angular momentum is at a faster rate, and, thus, for large impact parameters the energy loss is larger than that in the case of ELPL2, as seen in Fig. 9, *a*. The same features are reflected also in the calculated  $b$  dependence of variances  $\sigma_{\Delta E \Delta E}^2$  displayed in Fig. 9, *b*. The maximum kinetic energy loss is finally seen to be almost similar in all the three cases as for very small impact parameters the total time spent by the two ions within their interaction zone is quite large. A comparison of the experimental energy distribution data with the calculated results depicted in Fig. 10 shows that for smaller energy loss  $\Delta E$  up to around 50 MeV the DISLIM case leads to cross-section  $d\sigma/d\Delta E$  values which are several times larger than the experimental values. In contrast, the ELPL1 and ELPL2 cases are in better agreement with the data illustrating the significance of equilibration time. From an overall consideration the ELPL1 curve is considered to provide a better description of the experimental data, although for intermediate energy losses between 150 to 250 MeV the DISLIM case is seen to be closer to the data. As expected at even higher energies losses beyond  $\Delta E = 250$  MeV, the three cases yield similar results.

The results for the mean charge  $Z$  and the associated variances  $\sigma_{ZZ}^2$  have been drawn in Fig. 11, and the element distributions  $d\sigma/dZ$  are displayed in Fig. 12. Due to absence of repulsive diabatic potential in the dissipative limit case DISLIM, the ions spent more time in proximity of each other leading to larger diffusion as compared to other two cases ELPL1 and ELPL2. The mass asymmetry parameter  $\alpha$  is not coupled directly to the radial coordinate and, consequently, its variance  $\sigma_{ZZ}^2$  shown in Fig. 11, *b* does not exhibit the unrealistic growth observed in the case of other variances coupled to  $\sigma_{rr}^2$ . The results for the differential cross-section  $d\sigma/dZ$  in Fig. 12 exhibit maximum values 527.55 mb/ $Z$  unit at the mean charge  $Z = 36$  for the ELPL1, 178.15 mb/( $Z \cdot u$ ) at the mean element value  $Z = 37.5$  for the ELPL2, 1047.53 mb/( $Z \cdot u$ ) at the mean element value  $Z = 37$  for the DISLIM case,

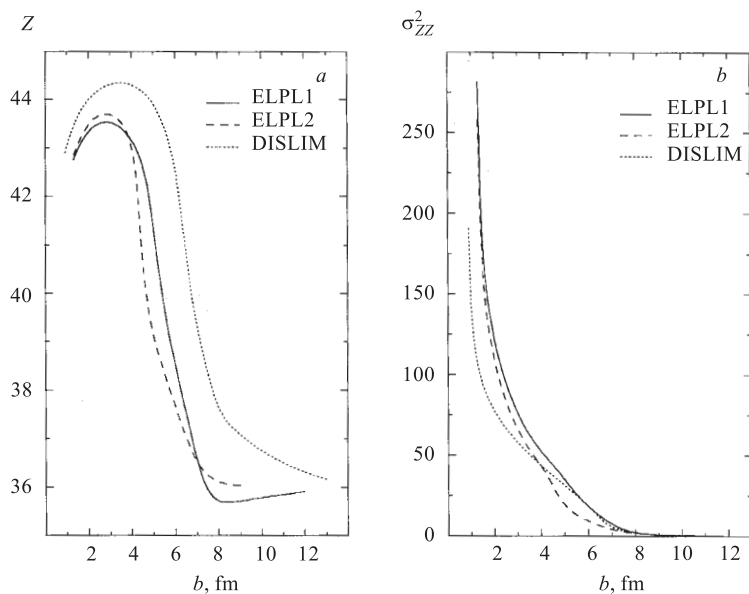


Fig. 11. The two plots, similar to Figs.7 and 9, correspond to the mean value of charge  $Z$  (a) and the associated variance  $\sigma_{ZZ}^2$  (b)

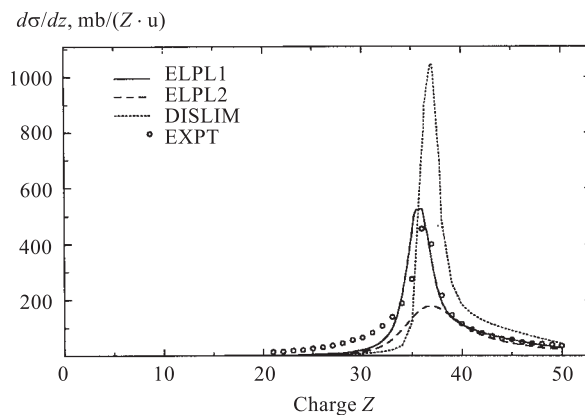


Fig. 12. Similar to Figs. 8 and 10, the plot shows a comparison of the calculated element distribution  $d\sigma/dZ$  with the experimental data [3]

respectively. A comparison with the experimental data shows that the position and magnitude of the maximum cross-section for the ELPL1 case is closest to the data. Thus, the results for the element distribution provide us a clear cut means to discriminate between the ELPL1 and ELPL2 cases, and enable us to conclude that the ELPL1 case provides the best description of the experimental data. This result supports our arguments for the exclusion of diabatic potential for the angular and grazing motions discussed earlier.

## CONCLUSIONS

We have studied the dissipative collisions between two heavy nuclei employing a macroscopic dynamical model within the framework of a multidimensional Fokker–Planck equation, wherein the reaction  $^{86}\text{Kr}$  (8.18 MeV/u) +  $^{166}\text{Er}$  has been used as a prototype to illustrate the memory effects.

During the fast approach of the colliding nuclei, the individual nucleons cannot follow the lowest possible adiabatic levels and the nucleonic wave functions remain almost unchanged. Such a diabatic behaviour gives rise to a large repulsive diabatic potential energy in addition to the adiabatic potential [6,8]. These initial correlations last during the intrinsic equilibration time  $\tau_{\text{int}}$  after which the complete phase space becomes relevant for the system. These considerations lead to the introduction of an explicitly time-dependent potential which smoothly connects to the adiabatic potential via the decay factor  $\chi(t)$ . The inclusion of such a dynamical potential in the transport theory extends its applicability to the initial fast stage of the collision process. This enables one to treat the non-Markovian effect (memory effects) in the nucleus–nucleus collision as has been demonstrated in the present calculations.

It is significant to note that the calculations with diabatic potential (ELPL1 and ELPL2) reproduce the negative deflection angles observed in the completely damped region. Similarly, the results for angular distribution  $d\sigma/d\theta_{\text{cm}}$ , energy distribution  $d\sigma/d\Delta E$  and element distribution  $d\sigma/dZ$  obtained in the ELPL1 case are found to be consistent with the measured data. The results of DISLIM calculations, in contrast, are not favoured by the measurements, which illustrates remarkably the dependence of the observables on the memory effects. A comparison of the experimental data for the element distribution  $d\sigma/dZ$  with calculations enables us to discriminate between the two slightly different elastoplastic cases, ELPL1 and ELPL2. It is found that the ELPL1 description is preferable to that of ELPL2. This is in accord to our belief that the diabatic potential may not be used for tangential or grazing collisions.

**Acknowledgements.** One of the authors (HLY) is deeply indebted to Prof. W. Nörenberg for initiating him to the subject during his stay at the GSI, Darmstadt, Germany, and for his continued interest and encouragement.

We are grateful to the Department of Science and Technology (DST), Government of India for financial support under the project No. SP/S2/K-28/97.

## REFERENCES

1. Weidenmüller H. A. // Prog. Part. Nucl. Phys. 1980. V. 3. P. 49.
2. Nörenberg W., Weidenmüller H. A. Introduction to the Theory of Heavy-Ion Collisions. Heidelberg: Springer, 1980.
3. Gobbi A., Nörenberg W. Heavy-Ion Collisions / Ed. R. Bock. Amsterdam: North-Holland, 1980. V. 2.
4. Schmidt K.-H., Morawek W. // Rep. Prog. Phys. 1991. V. 54. P. 949.
5. Nörenberg W. // Nucl. Phys. A. 1983. V. 409. P. 191; V. 400. P. 275.
6. Nörenberg W. // Phys. Lett. B. 1981. V. 104. P. 107.

7. *Reinhard P.-G., Yadav H.L., Toepffer C.* // Nucl. Phys. A. 1986. V. 458. P.301.
8. *Yadav H.L., Nörenberg W.* // Phys. Lett. B. 1982. V. 115. P. 180.
9. *Werner E. et al.* // Z. Phys. A. 1981. V. 299. P. 231.
10. *Pal S., Ganguly N.K.* // Nucl. Phys. A. 1981. V. 370. P. 175.
11. *Nörenberg W., Riedel C.* // Z. Phys. A. 1979. V. 290. P. 335.
12. *Bertsch G.F.* // Z. Phys. A. 1978. V. 289. P. 103.
13. *Landau L.* // Phys. Z. Sowjetunion. 1932. V. 1. P. 88; V. 2. P. 46;  
*Zener C.* // Proc. Roy. Soc. A. 1932. V. 137. P. 696.
14. *Lukasiak A., Cassing W., Nörenberg W.* // Nucl. Phys. A. 1984. V. 426. P. 181.
15. *Diaz-Torres A., Antonenko N.V., Schied W.* // Nucl. Phys. A. 1999. V. 652. P. 61;  
*Diaz-Torres A. et al.* // Phys. Lett. B. 2000. V. 481. P. 228.
16. *Barrett B.R., Shlomo S., Weidenmüller H.A.* // Phys. Rev. C. 1978. V. 17. P. 544.
17. *Ayik S., Wolschin G., Nörenberg W.* // Z. Phys. A. 1978. V. 286. P. 271.
18. *Möller P., Nix J.R.* // Nucl. Phys. A. 1977. V. 281. P. 354.
19. *Nix J.R.* Private communication.
20. *Schandera Ch. et al.* Verhandlungen der DPG, Spring Meeting, Karlsruhe, 1982. P. 1163;  
*de Boer J.* Private communication.
21. *Rudolf G. et al.* // Nucl. Phys. A. 1981. V. 367. P. 109.

Received on January 16, 2003.